Journal of Alloys and Compounds 508 (2010) 162–171

Contents lists available at ScienceDirect

Journal of Alloys and Compounds

journal homepage: www.elsevier.com/locate/jallcom

# Characterization investigations during mechanical alloying and sintering of Ni–W solid solution alloys dispersed with WC and $Y_2O_3$ particles

Aziz Genç*, M. Lütfi Öveçoğlu

*Particulate Materials Laboratories, Department of Metallurgical and Materials Engineering, Istanbul Technical University, Maslak, 34469 Istanbul, Turkey*

ARTICLE INFO

*Article history:*
Received 13 July 2010
Received in revised form 4 August 2010
Accepted 6 August 2010
Available online 19 August 2010

*Keywords:*
Mechanical alloying
Ni–W alloys
WC
$Y_2O_3$

ABSTRACT

Blended elemental Ni–30 wt.% W powders were mechanically alloyed (MA'd) for 1 h, 3 h, 6 h, 12 h, 24 h, 36 h and 48 h in a Spex mixer/mill at room temperature in order to investigate the effects of MA duration on the solubility of W in Ni and the grain size, hardness and particle size. Microstructural and phase characterizations of the MA'd powders were carried out using X-ray diffractometer (XRD), scanning electron microscope (SEM) and transmission electron microscope (TEM). On the basis of achieved saturation on the solid solubility, hardness and particle size, the Ni–30 wt.% W powders MA'd for 48 h were chosen as the matrix which was reinforced with different amounts of WC and/or with 1 wt.% $Y_2O_3$ particles. The reinforced powders were further MA'd for 12 h. The MA'd powders were sintered at 1300 °C for 1 h under Ar and $H_2$ gas flowing conditions. Microstructural characterizations of the sintered samples were conducted via XRD and SEM. Sintered densities were measured by using the Archimedes' method. Vickers microhardness tests were performed on both MA'd powders and the sintered samples. Sliding wear experiments were done in order to investigate wear behaviors of the sintered samples.



## 1. Introduction

Ni–W alloys are known to exhibit superior mechanical properties (high tensile strength and hardness), higher heat and wear resistance and also better corrosion behavior than elemental Ni [1,2]. In addition to their outstanding mechanical and chemical properties, Ni–W alloys have received attention as being potential candidates of an environmentally friendly substitute for hard chrome plating [3] and because of their enhanced catalytic activities [4]. Moreover, Ni–W alloys can be used as a substrate for high temperature superconductors [5].

Non-equilibrium compositions of Ni–W alloys can be fabricated using electrodeposition technique and MA [6–23]. Synthesis of Ni–W alloys by electrodeposition was first reported by Yamasaki et al. [6] and since then, there have been a quite number of studies which reported mechanical, tribological and chemical properties of the Ni–W alloys fabricated via electrodeposition with different W amounts and different deposition parameters [1,2,6–16]. Similar to electrodeposition, MA'd powders also exhibit extension of equilibrium solid solubility limits [17]. In addition to synthesizing equilibrium solid solutions, it has also been possible to synthesize non-equilibrium (metastable) supersaturated solid solutions by MA starting from blended elemental powders [17]. The equilibrium and non-equilibrium solubility of W in MA'd Ni–W alloys was reported by several researchers [18–23]. Aning et al. [20] stated that if the W content is greater than about 28 at.%, amorphization of the powders occurs. Nasu et al. [23] compared the structural features of the electrodeposited and MA'd Ni–20 at.% W alloys and indicated that the structures of MA'd Ni–W alloys are similar to those of the electrodeposited alloys however they contain small amounts of undissolved pure Ni and W in the investigated MA conditions. More recently, powder metallurgical routes and subsequent cold rolling have been utilized for Ni–W alloys to form cubic textures for superconductor applications [24–26].

Significant enhancements on the mechanical, tribological and chemical properties of electrodeposited Ni–W alloys have been achieved by co-deposition with different insoluble particles of SiC [27], $SiO_2$ [28], $Al_2O_3$ [29], $CeO_2$ [30], WC [31], $ZrO_2$ [32]. However, there are no reported investigations regarding the dispersion strengthening of Ni–W alloys fabricated via MA. In the present investigation, Ni–30 wt.% W alloys were produced via MA and sintering at 1300 °C for 1 h. Effects of MA durations on the solid solubility of W and the microstructure, particle size distribution and hardness of the MA'd powders were evaluated. WC and $Y_2O_3$ particles were added as dispersoids and their influences on the properties were investigated. Microstructural and physical properties of the sintered samples were investigated.

## 2. Experimental procedures

Elemental nickel (Ni) (Alfa Aesar™, 99.9% purity, 3–7 μm average particle size) and tungsten (W) (Eurotungstene™, 99.9% purity, 14 μm average particle size) and $Y_2O_3$ (Alfa Aesar™, 99.9% purity, 1 μm average particle size) and WC (Alfa Aesar™, 99.5% purity, 3.3 μm average particle size) powders were used in the present inves-

* Corresponding author. Tel.: +90 2122857347; fax: +90 2122853427.
*E-mail address:* agenc@itu.edu.tr (A. Genç).

0925-8388/$ – see front matter © 2010 Elsevier B.V. All rights reserved.
doi:10.1016/j.jallcom.2010.08.038

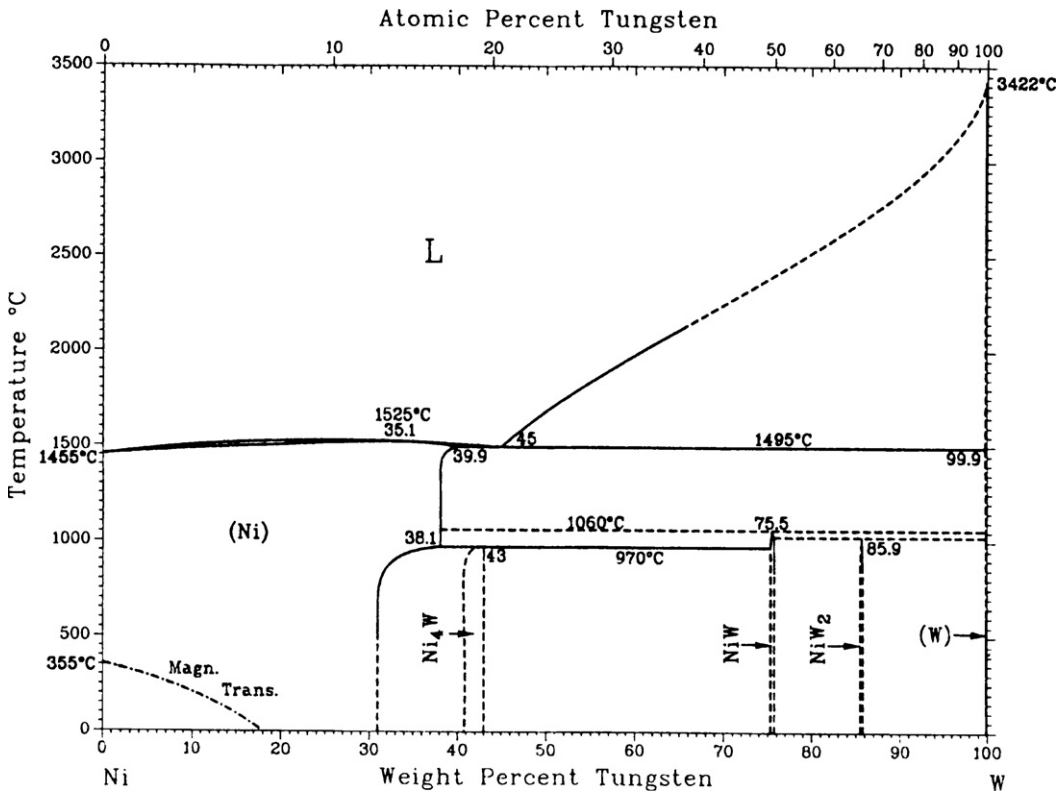


**Fig. 1.** The binary Ni–W phase diagram [35].

tigation. Ni and W powders were blended to constitute the composition Ni–30 wt.% W (hereafter referred to be as Ni30W) which were mechanically alloyed (MA'd) for different durations of 1 h, 3 h, 6 h, 12 h, 24 h, 36 h and 48 h using a Spex™ Duo Mixer/Mill 8000D with a speed of 1200 rpm in a tungsten carbide (WC) vial with WC balls having a diameter of 6.35 mm (1/4 in.). The vials were sealed inside a Plaslabs™ glove box under purified Ar gas (99.995% purity) to prevent oxidation during MA. The ball-to-powder weight ratio (BPR) was 10:1. 1 wt.% Stearic acid was used as a process control agent (PCA) to inhibit cold-welding and agglomeration during MA. WC powders were pre-milled for 24 h using the same conditions and had an average particle size distribution of about 180 nm after milling. Solid solubility of W in Ni was observed using a Bruker™ D8 Advance X-ray diffractometer (XRD) (Cu Kα radiation) on the basis of peak shifting and Vegard's law [33]. Pre-milled WC particles and $Y_2O_3$ particles were added to Ni30W powders MA'd for 48 h. Powder blends having the compositions of Ni30W, Ni30W–2.5 wt.% WC, Ni30W–5 wt.% WC, Ni30W–1 wt.% $Y_2O_3$, Ni30W–2.5 wt.% WC–1 wt.% $Y_2O_3$ and Ni30W–5 wt.% WC–1 wt.% $Y_2O_3$ (hereafter referred to be as Ni30W, Ni30W + 2.5WC, Ni30W + 5WC, Ni30W + $1Y_2O_3$, Ni30W + 2.5WC + $1Y_2O_3$ and Ni30W + 5WC + $1Y_2O_3$, respectively) were further MA'd for 12 h using the same conditions.

Powder particle size measurements were carried out in a Malvern™ Mastersizer Laser particle size analyzer. Microstructural characterization investigations of as-blended and MA'd powders were conducted using a Hitachi™ TM-1000 scanning electron microscope (SEM), Jeol™-JEM-EX2000 transmission electron microscope (TEM) and a Bruker™ D8 Advance XRD (Cu Kα radiation). Crystallite sizes and the retained strain of the MA'd powders were measured by using TOPAS 3 (Bruker™ AXS) software [34]. Vickers microhardness tests on the MA'd powders were performed using a Shimadzu™ microhardness tester under a load of 100 g for 10 s. Microhardness test result for each sample is the arithmetic mean of about 10 successive indentations and standard deviations.

MA'd powders were compacted in a 10 ton capacity APEX™ 3010/4 uni-action hydraulic press to obtain cylinder type compacts with a diameter of 12.75 mm under an uniaxial pressure of 400 MPa. The compacts were sintered in a Linn™ high temperature hydrogen furnace at 1300 °C under inert Ar (introduced between 20–650 °C and 900–1300 °C) and reducing $H_2$ (introduced between 650 °C and 900 °C) gas flowing conditions for 1 h. Microstructural characterizations of the sintered samples were carried out using a Bruker™ D8 Advance XRD and a Jeol™-JSM-5410 SEM equipped with a Noran™ 648D-1FSS EDS apparatus. Sintered densities were measured by using the Archimedes' method. Vickers microhardness tests on sintered samples were conducted using a Shimadzu™ microhardness tester under a load of 100 g for 10 s. The sliding wear experiments were conducted on a Tribotech™ Oscillating Tribotester using 6 mm alumina balls under an applied force of 10 N. The tests were conducted at room temperature in a laboratory atmosphere with a sliding speed of 10 mm/s, a stroke length of 5 mm and a sliding distance of 20 m. Abraded surfaces were characterized using a Veeco™ Dektak 6 M Stylus Profiler and test results are arithmetic mean of three different measurements for each sample.

## 3. Results and discussion

Fig. 1 shows the binary phase diagram of Ni–W [35]. As seen in Fig. 1, Ni–30 wt.% W alloy, which is equivalent to about Ni–12.2 at.% W is in the equilibrium solid solution phase.

### 3.1. Optimization of MA conditions

Fig. 2 shows the XRD patterns of the Ni30W powders MA'd for different durations. The XRD pattern of as-blended Ni30W pow-

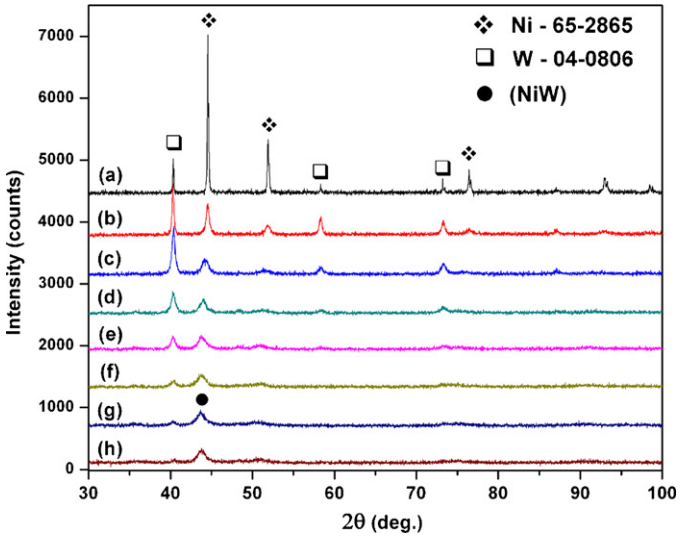


**Fig. 2.** XRD patterns of Ni30W powders in the (a) as-blended conditions and MA'd for: (b) 1 h, (c) 3 h, (d) 6 h, (e) 12 h, (f) 24 h, (g) 36 h and (h) 48 h.

**Table 1**
Properties of the MA'd Ni30W powders.

| Sample | W solution in Ni (at.%) | Grain size (nm) | Hardness ($HV_{0.1}$) | Particle size ($d_{0.5}$) (μm) |
|---|---|---|---|---|
| As-blended | – | 249 | 287 ± 102 | 19.609 |
| MA'd for 1 h | – | 36.3 | 383 ± 82 | 32.388 |
| MA'd for 3 h | 7.422 | 28.1 | 582 ± 88 | 18.178 |
| MA'd for 6 h | 10.628 | 16.8 | 703 ± 56 | 21.381 |
| MA'd for 12 h | 15.329 | 12.5 | 757 ± 38 | 14.183 |
| MA'd for 24 h | 17.826 | 11.8 | 823 ± 16 | 10.819 |
| MA'd for 36 h | 17.826 | 7.6 | 871 ± 37 | 11.659 |
| MA'd for 48 h | 17.864 | 7.4 | 902 ± 28 | 10.049 |

ders (Fig. 2a) reveals the presence of the characteristic peaks of the Ni phase which has a f.c.c. Bravais lattice and $Fm\bar{3}m$ space group with the lattice parameter of $a = 0.352$ nm [36] and the W phase which has a b.c.c. Bravais lattice and $Im\bar{3}m$ space group with the lattice parameter of $a = 0.316$ nm [37]. Likewise, the XRD pattern of Ni30W powders MA'd for 1 h (Fig. 2b) reveals the same Ni and W phases. Peak intensities decrease drastically after MA for 1 h due to the grain refinement of Ni. Further increase in MA duration results in further broadening of the peaks of both phases as a result of grain refinement and buildup strain during MA. Formation of (NiW) solid solution starts after MA for 3 h and increases with increasing MA duration where Ni peaks shift to greater d values as a consequence of increasing W amount in the Ni lattice (Fig. 2c). Concurrently, the intensity of the W peaks decrease with increasing MA durations as a result of the solution process. Table 1 gives the W solid solubility values in Ni with increasing MA duration calculated by using the Vegard's law [33] and the grain sizes of MA'd Ni30W powders calculated using the TOPAS 3 software. As seen in Table 1, in the initial stage of MA, an average size of 249 nm of Ni grains in the as-blended powders decrease significantly and become 36 nm after MA for 1 h, whereas no solid solution formation occurs at this stage. Grain size of Ni/(NiW) solid solution decreases systematically with increasing MA duration and the Ni30W powders MA'd for 48 h have an average crystallite size of 7.4 nm. The solubility of W in Ni also increases with increasing MA duration. 7.42 at.% W solubility for the Ni30W powders MA'd for 3 h increases to 17.82 at.% for those MA'd for 24 h. The solubility of W in Ni reaches a saturation value and becomes 17.86 at.% for the Ni30W powders MA'd for 48 h. Aning et al. [20] reported a similar saturation phenomenon in the MA'd Ni–15 at.% W alloys. It is worth noting that the lattice parameter of W also changes during processing due to extended solubility of 2.29 at.% Ni in the W lattice. Streletskii and Courtney [22] have also reported a solubility value of 1.7 at.% Ni in the W lattice after MA for 10 h. According to Ni–W binary phase diagram (Fig. 1) [35] Ni solubility in W is negligible, however, it is very well known that non-equilibrium (metastable) supersaturated solid solutions can be produced using MA [17–23]. As can be noticed, calculated W solution amounts are higher than the amount of W in the starting powder batches. The reason for these high W amounts could be due to WC contamination during MA. In order to determine the amount of WC contamination coming from the milling media, XRF measurements have been conducted and revealed the presence of 0.38 wt.% Co in the Ni30W powders MA'd for 36 h, which is equivalent to about 5.95 wt.% WC contamination. Even after assumption of the total decarburization of all the contaminated WC to W, calculated W values are still higher than the estimated W amounts, indicating that the possible penetration of WC into Ni lattice occurred in either WC form or $W_2C$ which formed during MA. Penetration of the $W_2C$ phase which has a hexagonal Bravais lattice and the lattice parameters of $a = 0.519$ nm and $c = 0.472$ nm [38] can cause shifting of Ni peaks to greater d values since the lattice parameters are larger than that of Ni ($a = 0.352$ nm).

Vickers microhardness results of the MA'd Ni30W powders are given in Table 1. A hardness value of $287 \pm 102\ HV_{0.1}$ for the as-blended Ni30W powders increases with increasing MA duration and reaches a maximum value of $902 \pm 28\ HV_{0.1}$ after MA for 48 h. Large standard deviations in the hardness values of the as-blended powders and for those during the initial stage of MA, i.e., 1 h and 3 h, can be attributed to the presence of both elemental Ni and W powders in their structure. It can be noticed from Table 1 that saturation on the hardness values is reached after MA for 36 h, which is quite similar to saturation of hardness values of Al matrix composite powders fabricated via MA [39]. According to Schuh et al. [10], both solid solution and grain-boundary hardening can contribute to the measured hardness of nano-crystalline Ni–W alloys fabricated via electrodeposition. On this basis, hardness of Ni–W alloys can be determined using Eq. (1):

$$H = H_0 + \Delta H_{ss} + \Delta H_{gb} \quad (1)$$

where $H_0$ is the intrinsic hardness of a high-purity single crystal Ni specimen, $\Delta H_{ss}$ is the increment of hardness resulting from solid solution strengthening, and $\Delta H_{gb}$ is the additional hardness due to grain refinement [10]. In the case of nano-crystalline Ni–W alloy powders fabricated via MA, strain hardening should also contribute to the strengthening of the composites. Calculation using TOPAS 3 software revealed a negligible strain value of 0.31% in the as-blended Ni30W powders, which increased up to 3.8% during MA process. These increases in the strain values could strongly affect the measured hardness values.

Fig. 3a–d shows the representative SEM/BEI micrographs of the Ni30W MA'd for different durations. Ni and W particles in the microstructure of Ni30W MA'd for 1 h are indexed in Fig. 3a. Cold-welding and flattening of ductile Ni particles take place during the initial stage of MA (Fig. 3a). As well as applied Vegard's law, an idea about the evaluation of solid solution formation can be gained by observing the distribution of white W particles in the SEM/BEI micrographs of the powders. Increasing MA duration, thereby increasing (NiW) solid solution formation, makes particles more brittle than elemental Ni, which results in fracturing of cold-welded and flattened particles. Fig. 3b shows the spheroidal agglomerates of Ni30W powders MA'd for 6 h with a diameter of about 10–20 μm. Inset figure in Fig. 3b is a close-up micrograph of a (NiW) agglomerate containing elemental W particles (indexed with a black arrow) in its microstructure. Fig. 3c shows the spheroidal agglomerates of Ni30W powders MA'd for 24 h with a diameter of about 10 μm. Moreover, compared to Ni30W powders MA'd for 6 h (Fig. 3b), fraction of elemental W particles decreases drastically after MA for 24 h (Fig. 3c). As seen in inset figure of Fig. 3d, elemental W particles are still present in the microstructure of the Ni30W powders MA'd for 48 h. Average particle size measurements are given in Table 1. As-blended Ni30W powders have an average particle size of 19.6 μm indicating the agglomeration of starting powders of Ni (average size of 7 μm) and W (average size of 14 μm). The characteristic tendency of cold-welding of ductile particles during MA causes an increase in particle size distribution at the initial stage of MA, where Ni30W powders MA'd for 1 h have an average particle size of 32.38 μm. Steady-state conditions between cold-welding and fracturing are achieved after MA for 24 h and further increasing of MA duration slightly changed the average particle size of the powders (Table 1). Thus, the mechanism of the evolution of particle size values, as stated by Suryanarayana [17], is quite similar to the mechanism of mechanical alloying of ductile materials where narrow particle size distribution caused by tendency of small particles to weld together and large particles to fracture under steady-state conditions.

The presence of elemental W and (NiW) solid solution phases in the Ni30W powders MA'd for 12 h is observed in the XRD pattern (Fig. 2e). Fig. 4a–c, however, shows the bright field, dark field

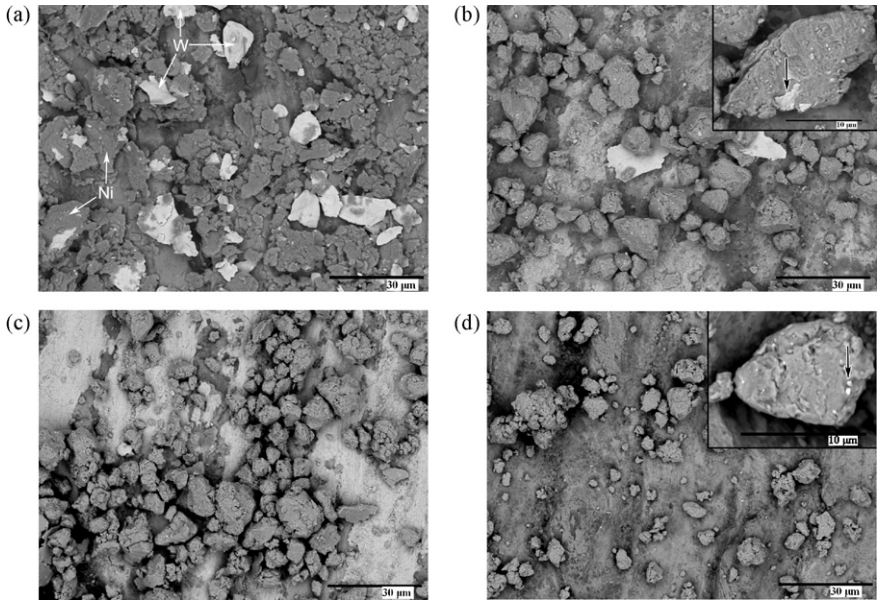


**Fig. 3.** Representative SEM/BEI micrographs of Ni30W powders: (a) MA'd for 1 h, (b) MA'd for 6 h, (c) MA'd for 24 h and (d) MA'd for 48 h.

and selected area diffraction pattern TEM micrographs indicating the presence of elemental Ni particles in the Ni30W powders MA'd for 12 h. A selected area diffraction pattern taken from the lower left particle in Fig. 4a presented in Fig. 4c and suggests that these particles ranging in size between 10 and 20 nm (indexed as Ni in Fig. 4a and b) are being composed of Ni. Very weak and/or almost amorphous like diffraction patterns taken from spherical particles in Fig. 4a. However, regarding their distributions in the microstructures and XRD patterns presented in Fig. 2, it is believed that these particles are being composed of (NiW) solid solution.

Fig. 5a and b shows the bright field TEM micrograph and a selected area diffraction pattern taken from the Ni30W powders MA'd for 48 h, respectively. As seen in halo diffraction pattern (Fig. 5b) taken from Fig. 5a, almost total amorphization of the powders takes place after MA for 48 h, which is also consistent with the XRD pattern presented in Fig. 2h. The diffusion and severe deformation during MA result in a substantial disappearance of grain boundaries (indexed with black arrows in Fig. 5a) and eventually amorphization.

### 3.2. The effects of WC and $Y_2O_3$ additions

On the basis of above presented steady-state achievement with observed saturation on the solid solution formation, particle and grain sizes and hardness values, Ni30W powders MA'd for 48 h have been chosen as the matrix to be further reinforced with WC and $Y_2O_3$ particles. Fig. 6a–f is the XRD patterns of Ni30W powders reinforced with WC and/or $Y_2O_3$ particles. Only the (NiW) solid solution peak is observed in the XRD pattern of the Ni30W powders MA'd for 60 h in total (Fig. 6a). As seen in Fig. 6b–f, XRD patterns of Ni30W powders reinforced with 2.5 wt.% and 5 wt.% WC and/or 1 wt.% $Y_2O_3$ particles are similar. The peaks of WC and $Y_2O_3$ cannot be observed probably due to their small amounts which disappeared in the amorphous background.

TEM investigations are conducted in order to get better understanding about the state of WC and $Y_2O_3$ particles in the MA'd NiW matrix. Fig. 7a–c is a series of bright field, dark field and selected area diffraction pattern TEM micrographs taken from Ni30W + 2.5WC powders. Fig. 7a shows the presence of black particles in the microstructure, which vary in size between 20 nm and 100 nm. Microstructural features of the spheroidal particles in Fig. 7a are quite similar to those of Fig. 5a, which possess an amorphous like microstructure. Fig. 7c is a selected area diffraction pattern taken from the lower right black particles in Fig. 7a indicating that these particles are being composed of the $W_2C$ phase which has a hexagonal Bravais lattice and the lattice parameters of $a = 0.519$ nm and $c = 0.472$ nm [38]. A careful check at other locations of the Ni30W + 2.5WC sample and quite a number of diffraction pat-

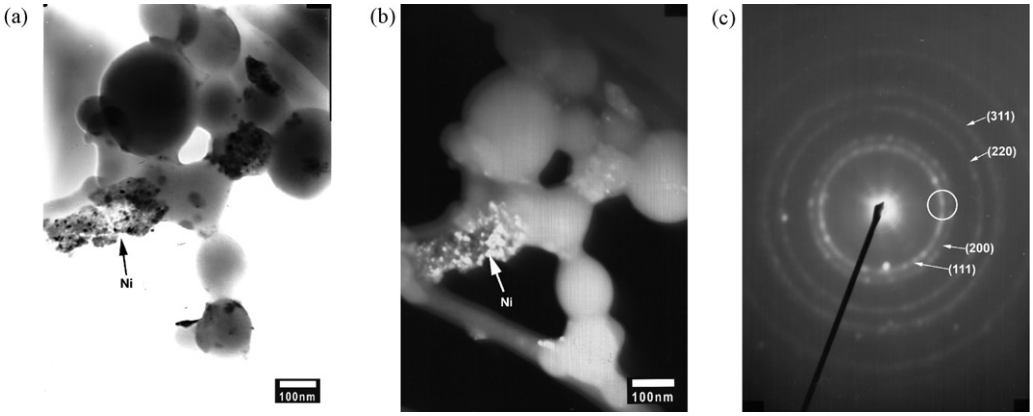


**Fig. 4.** TEM micrographs taken from the Ni30W powders MA'd for 12 h: (a) bright field image, (b) dark field image and (c) corresponding selected area diffraction pattern of Ni.

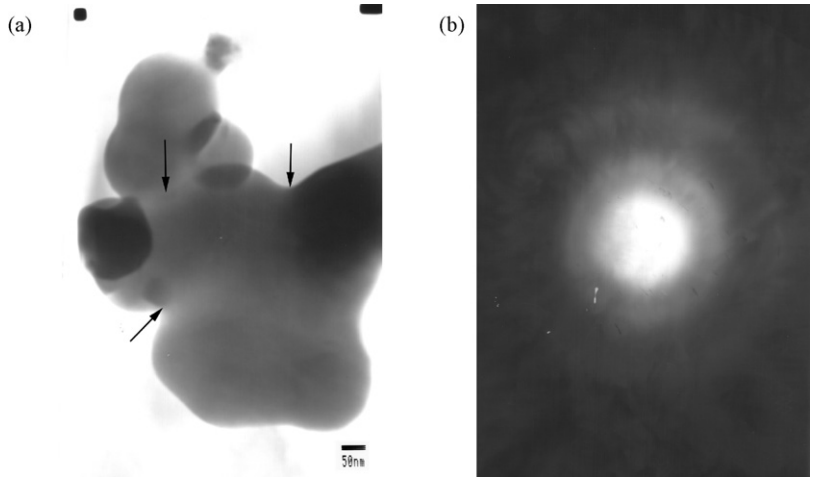


**Fig. 5.** TEM micrographs taken from Ni30W powders MA'd for 48 h: (a) bright field image, (b) selected area diffraction pattern indicating the amorphous structure.

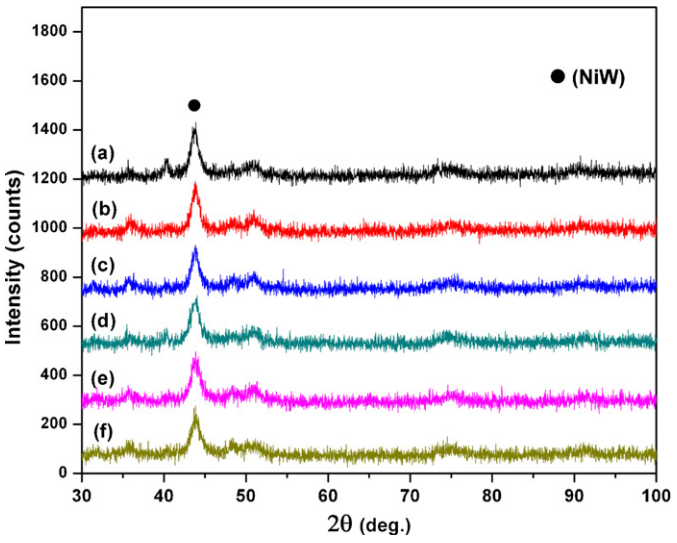


**Fig. 6.** XRD patterns of (a) Ni30W powders MA'd for 60 h in total, (b) Ni30W + 2.5WC, (c) Ni30W + 5WC, (d) Ni30W + $1Y_2O_3$, (e) Ni30W + 2.5WC + $1Y_2O_3$ and (f) Ni30W + 5WC + $1Y_2O_3$ powders.

terns taken from the sample also confirm the presence of the $W_2C$ phase, which formed due to transformation of WC. It is believed that, pre-milling of WC powders for 24 h and further milling with NiW powders for 12 h caused transformation of WC to $W_2C$. TEM observations of Fig. 7 present a strong contribution to the discussion about the distortion of Ni/(NiW) lattices with the penetration of $W_2C$ particles.

Fig. 8a and b is bright field and dark field TEM micrographs taken from the Ni30W + $1Y_2O_3$ powders showing spheroidal shaped particles varying in size between 20 nm and 80 nm. Corresponding electron diffraction pattern from the lower left black particles in Fig. 8a is shown in Fig. 8c. These spherical particles are unambiguously identified as being composed of $Y_2O_3$ phase which has a body centered cubic Bravais lattice with lattice parameter of $a = 1.0597$ nm [40].

### 3.3. Characterization of the sintered samples

Fig. 9a shows the XRD patterns of Ni30W, Ni30W + 2.5WC and Ni30W + 5WC samples revealing the presence of (NiW) solid solution peaks and a small diffraction peak from the {1 1 1} reflection plane of Ni. WC peaks cannot be observed probably due to the above mentioned penetration into Ni lattices and/or possible decarburization. It is evident from the peak shifts of the NiW solid solution phase in Fig. 9 that the solid solution extension of W in Ni does take place. Utilizing the least squares approximation method for peak shifts in combination with the Vegard's law [33], dissolved W amounts in the sintered Ni30W, Ni30W + 2.5WC and Ni30W + 5WC samples were calculated as 21.19 at.%, 23.51 at.% and 24.59 at.%, respectively. Increasing W amount in Ni30W sample can

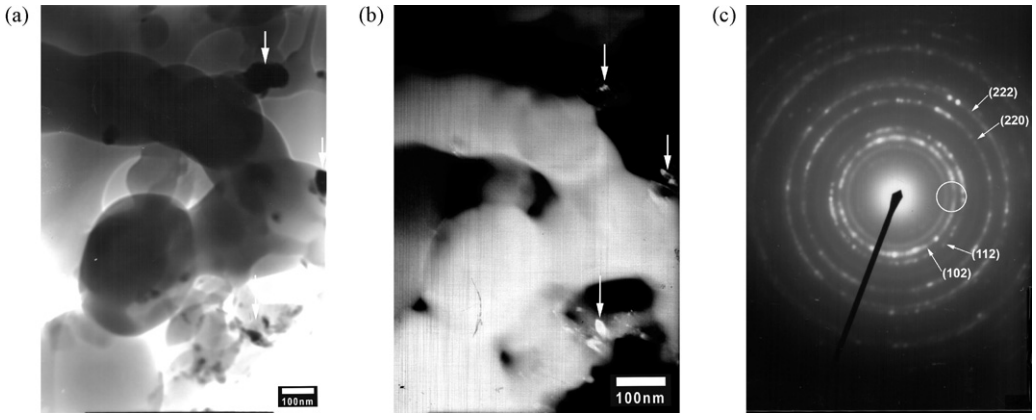


**Fig. 7.** TEM micrographs taken from Ni30W + 2.5WC powders: (a) bright field image, (b) dark field image and (c) corresponding selected area diffraction pattern of $W_2C$ phase.

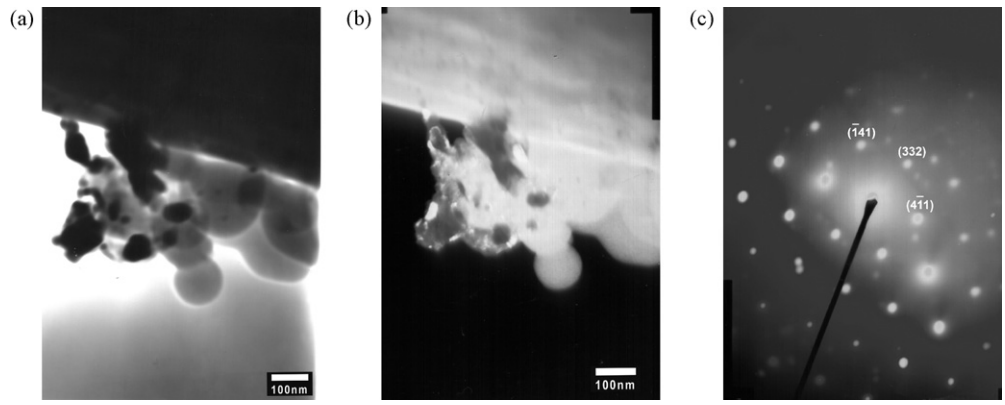


**Fig. 8.** TEM micrographs taken from Ni30W + 1$Y_2O_3$ powders: (a) bright field image, (b) dark field image and (c) corresponding selected area diffraction pattern of $Y_2O_3$ phase.

be attributed to the incorporation of W or WC particles into Ni lattices, which otherwise can clearly observed in the microstructures of the powders (inset figure in Fig. 3d). It is also obvious that the d values of (NiW) solid solution increase with increasing WC contents, which supports the hypothesis about WC penetration into the Ni lattice. Fig. 9b shows the XRD patterns of Ni30W + 1$Y_2O_3$, Ni30W + 2.5WC + 1$Y_2O_3$ and Ni30W + 5WC+ 1$Y_2O_3$ samples and reveals similar features with Fig. 9a, where only the peaks of (NiW) solid solution and a small peak of Ni are observed. Dissolved W amounts in the Ni30W + 1$Y_2O_3$, Ni30W + 2.5WC + 1$Y_2O_3$ and Ni30W + 5WC+ 1$Y_2O_3$ samples are predicted as 21.19 at.%, 22.35 at.% and 24.59 at.%, respectively. As seen in both Fig. 9a and b no intermetallic phases were formed between Ni and W. The expectation about diffusion of W from supersaturated metastable (NiW) solid solution did not take place [41], yet a small Ni peak was observed in the XRD patterns. It is believed that the presence of WC/$W_2C$ along with W in Ni lattice, may somehow prevent the W diffusion from Ni lattice during sintering. However, there is no evidence to support this phenomenon.

Fig. 10a–f is a series of SEM micrographs of the sintered Ni30W samples reinforced with WC and/or $Y_2O_3$. SEM micrographs of the sintered Ni30W (Fig. 10a), Ni30W + 2.5WC (Fig. 10b) and Ni30W + 5WC (Fig. 10c) samples reveal a similar microstructural feature with uniform contrast and having almost no open porosity. SEM micrograph of the sintered Ni30W + 1$Y_2O_3$ sample (Fig. 10d) reveals the distribution of submicron/micron sized particles in the microstructure. On the basis of EDS scans, particles having a chemical composition of 65.56 wt.% Ni, 25.53 wt.% W and 8.89 wt.% Y are indexed as Y-rich particles in Fig. 10d. SEM micrographs of the sintered Ni30W + 2.5WC + 1$Y_2O_3$ sample (Fig. 10e), Ni30W + 5WC + 1$Y_2O_3$ sample (Fig. 10f) also show the presence of these particles in the microstructures. No distinguished contrast regions implying the presence of WC/$W_2C$ particles as different phases were observed in the SEM micrographs of the sintered Ni30W + 2.5WC (Fig. 10b), Ni30W + 5WC (Fig. 10c), Ni30W + 2.5WC + 1$Y_2O_3$ sample (Fig. 10e) and Ni30W + 5WC + 1$Y_2O_3$ (Fig. 10f) samples probably due to the above mentioned penetration of WC/$W_2C$ particles into the Ni lattice.

Sintered samples were fractured manually in order to gain better comprehension about the microstructural features in the bulk of the samples. Fig. 11a–g is representative fracture surface SEM micrographs of the sintered Ni30W samples reinforced with WC and/or $Y_2O_3$. Fig. 11a is a fracture surface SEM/SEI micrograph taken from the sintered Ni30W sample showing intergranular fracturing features with elongated regions during fracturing, which suggest that sintered Ni30W sample possesses ductile characteristics. Fig. 11b is the corresponding BEI micrograph of Fig. 11a, revealing uniform contrast indicating the presence of one particular phase in the microstructure. On the basis of EDS scans taken from Fig. 11a and b, sintered Ni30W sample have the overall chemistry of 68.14 wt.% Ni and 31.86 wt.% W. As seen in Fig. 10a and b, the (NiW) grain sizes in the sintered Ni30W sample vary between 1 μm and 4 μm. Fig. 11c shows the fracture

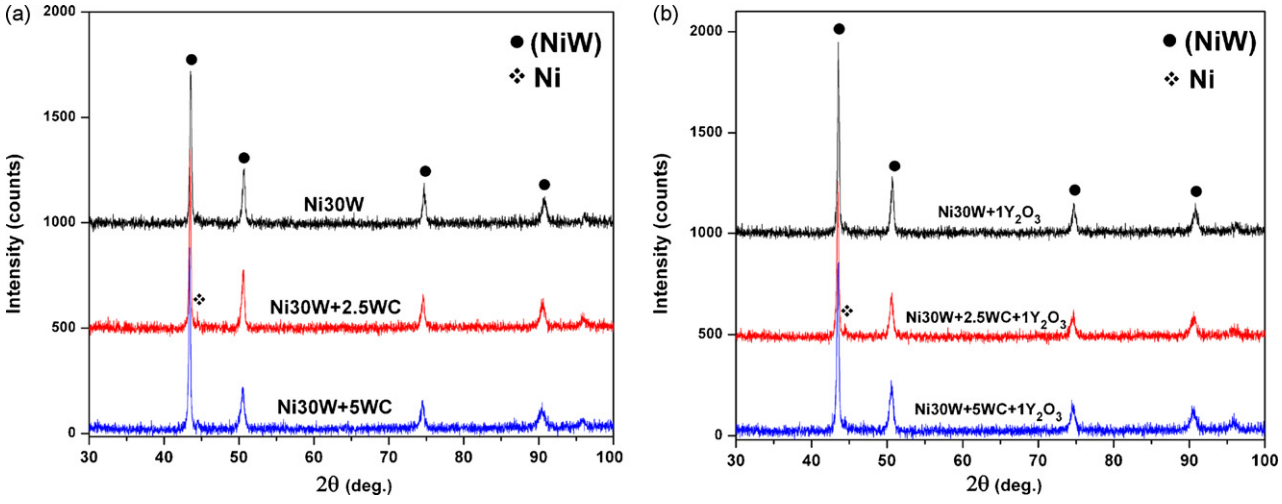


**Fig. 9.** XRD patterns of the sintered samples: (a) Ni30W samples reinforced with different amounts of WC and (b) Ni30W samples reinforced with $Y_2O_3$ and WC particles.

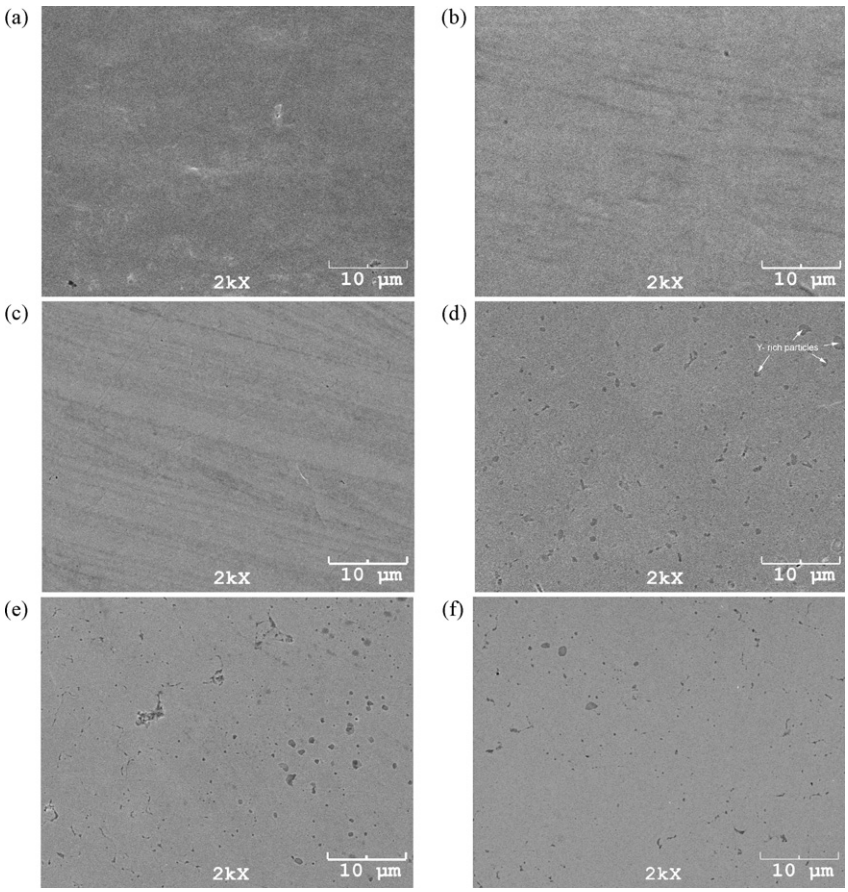


**Fig. 10.** SEM micrographs of the sintered Ni30W samples reinforced with WC and/or Y2O3: (a) Ni30W, (b) Ni30W + 2.5WC, (c) Ni30W + 5WC, (d) Ni30W + 1Y2O3, (e) Ni30W + 2.5WC + 1Y2O3 and (f) Ni30W + 5WC + 1Y2O3 samples.

surface SEM micrograph taken from the sintered Ni30W + 2.5WC sample. Although surface SEM micrograph of the same sample (Fig. 10b) has uniform contrast, careful observations conducted on the bulk of the sample revealed the presence of "pomegranate-like" regions in the microstructure where spherical particles having sizes between 0.1 μm and 1 μm are surrounded by the matrix. Inset figure in Fig. 11c shows higher magnification SEM micrograph of the pomegranate-like regions. We believe that the formation of these "pomegranate-like" regions result from consecutive mechanisms in the microstructure during MA and sintering. Firstly, the pre-milled WC particles with average particles size of 180 nm are surrounded by the matrix (NiW) phase during the initial stages of MA, which prevent the homogeneous distribution of WC particles in the microstructure. As MA progresses, the (NiW) and WC particles combine to produce ductile agglomerates which remain intact during MA. During sintering, simultaneous decarburization and growth of these particles take place in all composite agglomerates resulting in a "pomegranate-like" morphology. To test the validity of the decarburization step of the above proposed formation mechanism, EDS scans were taken from the spheroidal particles of this "pomegranate-like" region shown in Fig. 11c. These scans of the Ni30W + 2.5WC sample revealed that these particles are composed of 51.04 ± 6.19 wt.% Ni and 48.94 ± 6.18 wt.% W. Fig. 11d shows the distribution of these "pomegranate-like" regions in the fracture SEM microstructure of the sintered Ni30W + 5WC sample, indicating that increasing WC amount increases the volume fraction of these regions in the microstructure. EDS scans taken from the spheroidal particles in Fig. 11d revealed that these particles have an overall chemistry of 39.42 ± 6.53 wt.% Ni and 60.57 ± 6.53 wt.% W. The distinguished feature of the particles of Ni30W + 2.5WC and Ni30W + 5WC samples is their W amount, which increases with increasing WC content. EDS spectra analysis indicates the presence of negligible amounts of C in the microstructures of these particles suggesting the decarburization of the WC/$W_2C$ phases took place during sintering. In a previous study [42], the decarburization of TiC particles during sintering was reported, which attributed to the presence of oxygen in the MA'd powders. Here, the transformation of WC to $W_2C$ after reacting with W takes place during MA and the decarburization of the $W_2C$ occurs during sintering. As seen in the SEM micrographs of Ni30W + 2.5WC + 1$Y_2O_3$ sample (Fig. 11f) and Ni30W + 5WC + 1$Y_2O_3$ sample (Fig. 11g), the above mentioned "pomegranate-like" regions are not present probably due to the fact that addition of hard $Y_2O_3$ particles increases the fracturing mechanism during MA providing the homogeneous distribution of the WC particles in the microstructure.

Relative density values, microhardness values and wear amounts of the sintered samples are presented in Table 2. As seen in Table 2, relative density values of the sintered Ni30W samples decrease with increasing WC amounts, where 97.84 wt.% relative

**Table 2**
Properties of the sintered samples.

| Sample | Relative density (%) | Hardness ($HV_{0.1}$) | Wear ($mm^3$ $N^{-1}$ $m^{-1}$) × $10^{-5}$ |
|---|---|---|---|
| Ni30W | 97.84 | 367 ± 21 | 7.11 ± 2 |
| Ni30W + 2.5WC | 96.13 | 440 ± 34 | 5.951 ± 0.72 |
| Ni30W + 5WC | 91.38 | 533 ± 27 | 2.706 ± 0.52 |
| Ni30W + 1$Y_2O_3$ | 86.61 | 301 ± 15 | 8.414 ± 0.28 |
| Ni30W + 2.5WC + 1$Y_2O_3$ | 93.41 | 410 ± 28 | 6.875 ± 0.43 |
| Ni30W + 5WC + 1$Y_2O_3$ | 93.26 | 453 ± 27 | 4.336 ± 0.69 |

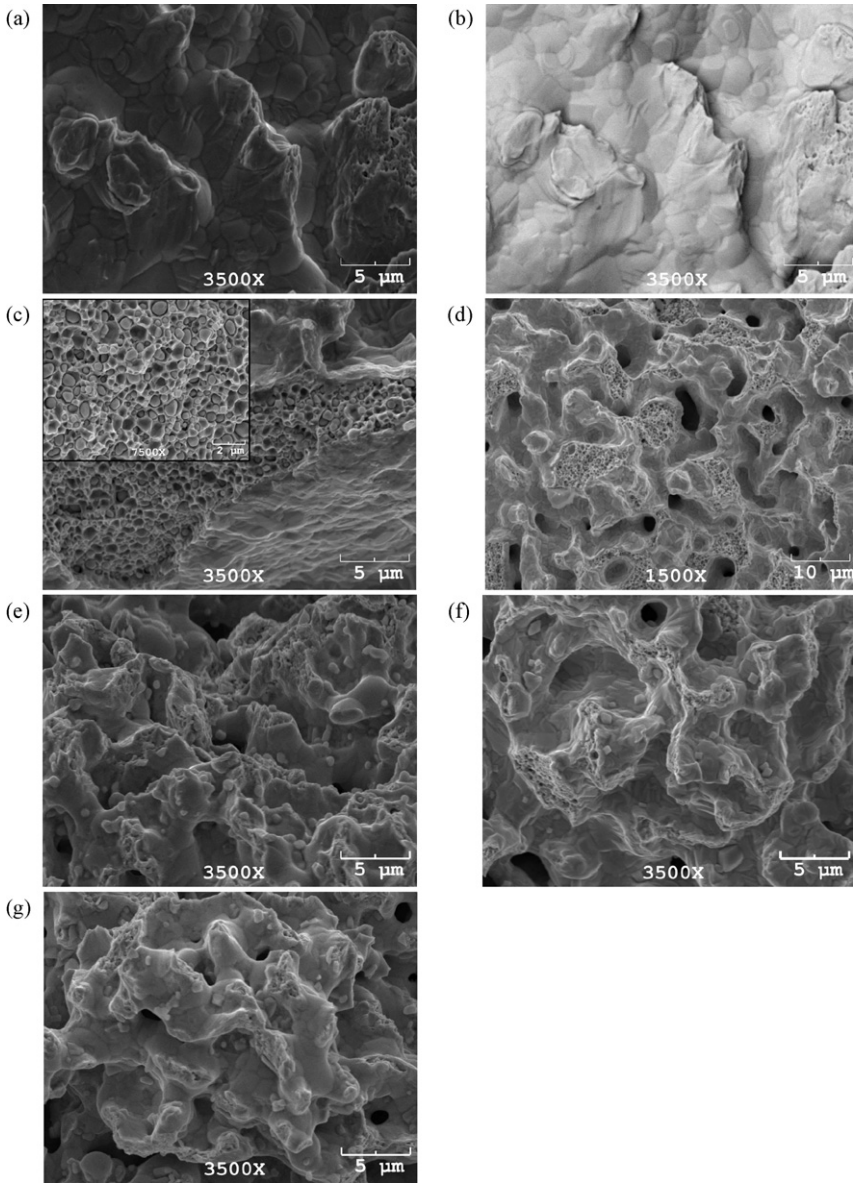


**Fig. 11.** SEM micrographs of the fracture surface of sintered Ni30W samples reinforced with WC and/or Y2O3: (a) Ni30W, (c) Ni30W + 2.5WC, (d) Ni30W + 5WC, (e) Ni30W + 1Y2O3, (f) Ni30W + 5WC + 1Y2O3 and (g) Ni30W + 5WC + 1Y2O3 samples, (b) is the corresponding BEI micrograph of (a). Inset figure in (c) is the higher magnification image showing "pomegranate-like" structure in the Ni30W + 2.5WC sample.

density value of the sintered Ni30W sample decrease to 91.38 wt.% for the sintered Ni30W + 5WC sample. Addition of 1 wt.% $Y_2O_3$ to Ni30W drastically decreases the relative density value of the sample, i.e., a relative density value of 86.61 wt.% is measured for the sintered Ni30W + 1$Y_2O_3$ sample. Further addition of WC particles along with $Y_2O_3$ increases the relative density values compared to the Ni30W + 1$Y_2O_3$ sample. The sintered Ni30W + 2.5WC + 1$Y_2O_3$ and Ni30W + 5WC + 1$Y_2O_3$ samples have respective relative density values of 93.41 wt.% and 93.26 wt.%.

Also seen in Table 2, microhardness values of the MA'd powders decrease drastically during sintering. A hardness value of 902 HV for the Ni30W powders MA'd for 48 h (Table 1) decrease to 367 HV for the sintered Ni30W sample fabricated from the powders MA'd for 60 h in total (Table 2). This is expected since different hardening mechanisms such as grain-boundary strengthening and strain hardening are no longer effective as much as they were in the MA'd powders. It is obvious that sintering led to considerable grain growth, where nanometer scale size of the Ni30W grains in the MA'd powders (Table 1) grew to about 1 μm and 4 μm in size in the sintered Ni30W sample (Fig. 11a). As reported by Robertson et al. [43], hardness values of the electrodeposited Ni samples are significantly affected by the grain sizes of the samples. In their study, electrodeposited Ni samples having average grain sizes of 10 μm, 100 nm and 10 nm had the respective hardness values of 140 HV, 300 HV and 650 HV [43]. Moreover, relieving of the retained strain took place during sintering and as a result the strain values of the sintered samples are quite negligible. Hardness values of the sintered Ni30W sample increases with increasing WC amount. Despite its lower density than the Ni30W sample, the sintered Ni30W + 5WC sample has a microhardness value of 533 HV (Table 2). Microhardness value of the sintered Ni30W sample decrease with the addition of 1 wt.% $Y_2O_3$ and becomes 302 HV for the sintered Ni30W + 1$Y_2O_3$ sample. Although an increment is expected in microhardness values with the addition of hard $Y_2O_3$ particles, low relative density value could be responsible for the decrease in the microhardness value of the Ni30W + 1$Y_2O_3$ sample. Ni30W + 2.5WC + 1$Y_2O_3$ and Ni30W + 5WC + 1$Y_2O_3$ samples have respective microhardness values of 410 HV and 453 HV,

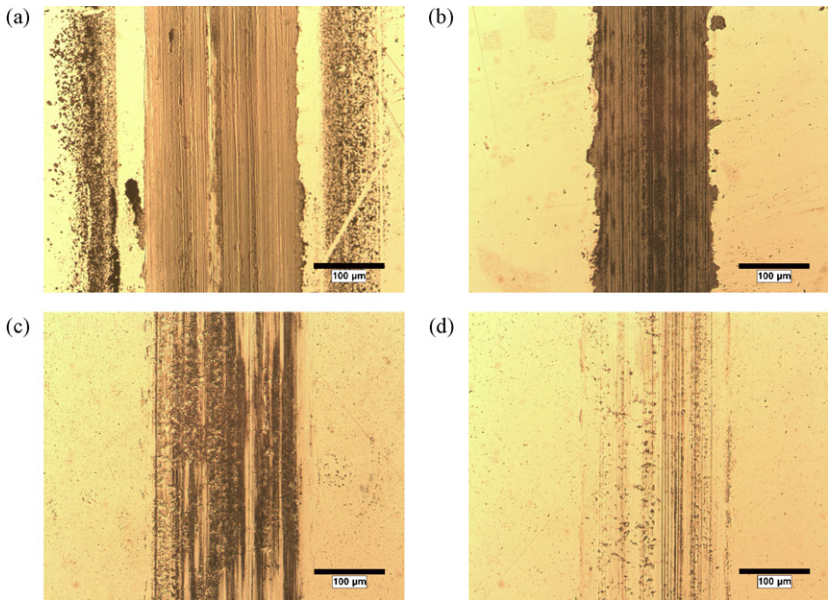


**Fig. 12.** Representative optical micrographs of the worn surfaces of: (a) Ni30W, (b) Ni30W + 5WC, (c) Ni30W + 1$Y_2O_3$ and (d) Ni30W + 5WC + 1$Y_2O_3$ samples.

which are unexpectedly lower than the microhardness values of the Ni30W + 2.5WC and Ni30W + 5WC samples. Formation of "pomegranate-like" regions in the sintered Ni30W samples reinforced with WC might be the reason for their relatively higher hardness values compared to those of the samples reinforced with both WC and $Y_2O_3$.

Wear amounts of the sintered samples are also listed in Table 2. The wear results given in Table 2 are the results obtained by measuring the length and the depth of the wear stroke and they are based on the assumption of the homogeneous wear in all 5 mm stroke length. For this reason, average values of three different measurements and standard deviations are presented as wear results. As shown in Table 2, the wear resistance of the Ni30W sample increases with increasing WC amounts. However, on the basis of these values, addition of $Y_2O_3$ particles has almost no effect on wear resistances of the sintered samples. Fig. 12a–d is representative optical micrographs taken from the worn surfaces of the sintered samples in order to reveal the wear characteristics of the samples. As seen in these figures, width of the wear stroke decreases with the addition of 5 wt.% WC and wear characteristics are almost the same both in the sintered Ni30W (Fig. 12a) and Ni30W + 5WC (Fig. 12b) samples. It is obvious from the micrographs of Fig. 12 that the addition of $Y_2O_3$ particles increases the resistance to scratch abrasion. Although, profilometry measurements seem to be logical for the sintered Ni30W samples reinforced with different amounts of WC particles, the addition of $Y_2O_3$ particles clearly changes the wear mechanism from adhesive to abrasive (Fig. 12c). The surface of the sintered Ni30W and Ni30W + 5WC samples were flattened out due to material removal from the sample during sliding wear experiments. However, the addition of $Y_2O_3$ particles might have caused mild abrasive wear damage. As seen in Fig. 12d, Ni30W sample reinforced with both 5 wt.% WC and 1 wt.% $Y_2O_3$ particles are quite resistant to wear under given sliding wear conditions. Although the coupled effects of reinforcing with both WC and $Y_2O_3$ particles cannot be clearly distinguished in the microhardness values, wear results indicate that they are much better effective if used together.

## 4. Summary and conclusions

The present study reports on the solid solution formation of Ni–30 wt.% W alloys and those reinforced with WC and $Y_2O_3$ particles fabricated via mechanical alloying and sintering. The effects of MA alloying duration on the solubility of W in Ni were investigated. A maximum W solubility in Ni was achieved in the Ni–30 wt.% W powders MA'd for 48 h. Microhardness values of the Ni–30 wt.% W powders increased systematically with increasing MA durations as a consequence of W solubility, grain refinement and strain hardening. The Ni–30 wt.% W powders MA'd for 48 h were reinforced with WC and/or $Y_2O_3$ particles which further MA'd together for 12 h. The MA'd powders were sintered at 1300 °C for 1 h under Ar, $H_2$ gas flowing conditions and the microstructural and physical properties of the sintered samples were characterized.

On the basis of the results of the present investigations, the following conclusions can be drawn:

(1) XRD patterns of the MA'd powders revealed the evaluation of Ni and W phases and formation of (NiW) solid solution phase and a maximum W dissolution value of 17.86 at.% was calculated for the Ni–30 wt.% W (Ni30W) powders MA'd for 48 h.
(2) A microhardness value of 287 HV for the as-blended Ni30W powders increased to 902 HV after MA for 48 h as a consequence of W solubility, grain refinement and strain hardening.
(3) SEM investigations on the MA'd Ni30W powders revealed the microstructural evolution of the MA'd powders and indicated the presence of elemental W particles even after MA for 48 h.
(4) TEM investigations on the Ni30W powders MA'd for 12 h revealed the presence of elemental Ni nanoparticles and amorphization of the powders after MA for 48 h. Nano-crystalline $W_2C$ and $Y_2O_3$ particles are also observed via TEM investigations
(5) XRD patterns of the sintered samples revealed the presence of (NiW) solid solution phase and a small peak of elemental Ni, whereas no intermetallic phases of Ni and W were formed during sintering.
(6) SEM micrographs of the sintered samples were consistent with the XRD patterns where an uniform contrast were formed. However, fracture surface SEM micrographs of the sintered Ni30W + 2.5WC and Ni30W + 5WC samples revealed the formation of "pomegranate-like" regions between the (NiW) matrix and the particles having higher W amounts than the matrix.
(7) A relative density value of 97.84% is achieved for the sintered Ni30W sample. Relative densities decreased with increasing

amount of WC reinforcements. Moreover, addition of 1 wt.% $Y_2O_3$ drastically decreased to relative density to 86.61%. Microhardness values of the MA'd powders decrease drastically during sintering. Increasing WC amounts increased the microhardness.

(8) On the basis of sliding wear experiments, the coupled effects of reinforcing with both WC and $Y_2O_3$ particles are revealed indicating that they are much better effective if used together.

In overall, considering the reported results of the present investigation, Ni–W alloys reinforced with WC and $Y_2O_3$ particles fabricated via mechanical alloying and sintering can be potential candidates for different structural applications.

## Acknowledgements

The authors would like to express their gratitude to State Planning Organization (DPT) for funding the project entitled "Advanced Technologies in Engineering" with the project number 2001K120750 out of which the main infrastructure of the Particulate Materials Laboratories was founded.

## References

[1] K.R. Sriraman, S.G.S. Raman, S.K. Seshadri, Mater. Sci. Eng. A 418 (2006) 303–311.
[2] N. Eliaz, T.M. Sridhar, E. Gileadi, Electrochim. Acta 50 (2005) 2893–2904.
[3] M. Osada, K. Maeda, Y. Kawamoto, Y. Shimizu, T. Nishimura, S. Yamaharu, U.S. Patent No. 6,773,247 (2004).
[4] M. Metikos-Hukovic, Z. Grubac, N. Radic, A. Tonejc, J. Mol. Catal.: A Chem. 249 (2006) 172–180.
[5] Y.X. Zhou, R. Naguib, H. Fang, K. Salama, Supercond. Sci. Technol. 17 (2004) 947–953.
[6] T. Yamasaki, P. Schlossmacher, K. Ehrlich, Y. Ogino, Nanostruct. Mater. 10 (1998) 375–388.
[7] O. Younes, L. Zhu, Y. Rosenberg, Y. Shacham-Diamand, E. Gileadi, Langmuir 17 (2001) 8270–8275.
[8] T. Yamasaki, Scr. Mater. 44 (2001) 1497–1502.
[9] L. Zhu, O. Younes, N. Ashkenasy, Y. Shacham-Diamand, E. Gileadi, Appl. Surf. Sci. 200 (2002) 1–14.
[10] C.A. Schuh, T.G. Nieh, H. Iwasaki, Acta Mater. 51 (2003) 431–443.
[11] Y. Wu, D.-Y. Chang, D.-S. Kim, S.-C. Kwon, Surf. Coat. Technol. 162 (2003) 269–275.
[12] H. Iwasaki, K. Higashi, T.G. Neigh, Scrip. Mater. 50 (2004) 395–399.
[13] D.B. Lee, J.H. Ko, S.C. Kwon, Mater. Sci. Eng. A 380 (2004) 73–78.
[14] Z. Galikova, M. Chovancova, V. Danielik, Chem. Pap. 60 (5) (2006) 353–359.
[15] M.D. Obradovic, G.Z. Bosnjakov, R.M. Stevanovic, M.D. Maksimovic, A.R. Despic, Surf. Coat. Technol. 200 (2006) 4201–4207.
[16] A.J. Detor, C.A. Schuh, Acta Mater. 55 (2007) 371–379;
A.J. Detor, C.A. Schuh, Acta Mater. 55 (2007) 4221–4232.
[17] C. Suryanarayana, Prog. Mater. Sci. 46 (2001) 1–184.
[18] I.S. Polkin, E. Kaputkin, A.B. Borzov, in: F.H. Froes, J.J. de Barbadillo (Eds.), Structural Applications of Mechanical Alloying, ASM International, Materials Park, OH, 1990, pp. 251–256.
[19] J. Zbiral, G. Jangg, G. Korb, Mater. Sci. Forum. 88/90 (1992) 19–26.
[20] A.O. Aning, Z. Wang, T.H. Courtney, Acta Metall. Mater. 41 (1993) 165–174.
[21] S. Mi, T.H. Courtney, Scripta Mater. 38 (1998) 637–644.
[22] A.N. Streletskii, T.H. Courtney, Mater. Sci. Eng. A 282 (2000) 213–222.
[23] T. Nasu, M. Sakurai, T. Kamiyama, T. Usuki, O. Uemura, K. Tokimitsu, T. Yamasaki, Mater. Sci. Eng. A 375/377 (2004) 163–170.
[24] Y. Zhao, H.L. Suo, M. Liu, D. He, Y.X. Zhang, L. Ma, M.L. Zhou, Acta Mater. 55 (2007) 2609–2614.
[25] P.P. Bhattacharjee, R.K. Ray, N. Tsuji, Acta Mater. 57 (2009) 2166–2179.
[26] Y. Zhao, H.L. Suo, Y.H. Zhu, J.C. Grivel, M. Gao, L. Ma, et al., Acta Mater. 57 (2009) 773–781.
[27] Y.W. Yao, S. Yao, L. Zhang, H. Wang, Mater. Lett. 61 (2007) 67–70.
[28] Y.W. Yao, Anti-Corros. Method. Mater. 54/6 (2007) 336–340.
[29] Y.W. Yao, Surf. Eng. 24/3 (2008) 226–229.
[30] B. Han, X. Lu, Surf. Coat. Technol. 202 (2008) 3251–3256.
[31] Y. Boonyongmaneerat, K. Saengkiettiyut, S. Saenapitak, S. Sangsuk, Surf. Coat. Technol. 203 (2009) 3590–3594.
[32] F.Z. Yang, L. Huang, S.K. Xu, S.M. Zhou, Acta Physico-Chim. Sinica 25/5 (2009) 864–868.
[33] L. Vegard, Zeitschrift fur Kristallographie 67 (1928) 239.
[34] A.A. Kern, A.A. Coelho, TOPAS 3 (BRUKER AXS), 2006, www.brukeraxs.com.
[35] T.B. Massalski, Binary Alloy Phase Diagrams, 2nd ed., ASM, Metals Park, OH, 1990.
[36] PowderDiffraction Files: Card No. 65-2865, database edition, The International Centre for Diffraction Data (ICDD).
[37] PowderDiffraction Files: Card No. 04-0806, database edition, The International Centre for Diffraction Data (ICDD).
[38] PowderDiffraction Files: Card No. 79-0743, database edition, The International Centre for Diffraction Data (ICDD).
[39] M.L. Öveçoğlu, W.D. Nix, Int. J. Powder Metall. 22 (1986) 17–30.
[40] Powder Diffraction Files: Card No. 71-5970, database edition, The International Centre for Diffraction Data (ICDD).
[41] R. Juskenas, I. Valsiunas, V. Pakstas, R. Giraitis, Electrochim. Acta 54 (2009) 2616–2620.
[42] A. Genç, S. Coşkun, M.L. Öveçoğlu, Int. J. Refract. Met. Hard Mater. 28 (2010) 451–458.
[43] A. Robertson, U. Erb, G. Palumbo, Nanostruct. Mater. 12 (1999) 1035–1040.